



Spatially-Resolved Insights Into Local Activity and Structure of Ni-Based CO₂ Methanation Catalysts in Fixed-Bed Reactors

Marc-André Serrer⁺,^[a, b] Matthias Stehle⁺,^[a] Mariam L. Schulte,^[a, b] Heino Besser,^[c] Wilhelm Pfleging,^[c] Erisa Saraçi,^[a, b] and Jan-Dierk Grunwaldt^{*[a, b]}

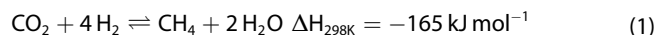
On a Ni/Al₂O₃ and a Ni-Fe/Al₂O₃ catalyst spatial concentration and temperature profiles were determined that occur along the axial direction of the catalyst bed. They were correlated to structural gradients under reaction conditions to elucidate the local dependency of catalyst structure on reaction-induced changes of the gas phase. The quantitative concentration and temperature profiles revealed a hotspot in the first third part of the fixed-bed, which led to by-product formation of CO. Complementary structural information obtained by spatially-resolved quick X-ray absorption spectroscopy unraveled a strong impact of reaction-induced gradients in gas phase on

the oxidation state of Fe with a higher oxidation state towards the end of the catalyst bed, while Ni was only slightly affected. Diffuse reflectance infrared Fourier transform spectroscopy further revealed that addition of Fe to a Ni/Al₂O₃ catalyst reduces the amount of adsorbed CO species. Hence, Fe hampers blocking of active Ni⁰ sites by CO and preserves a high fraction of reduced Ni species. Furthermore, an alternative reaction pathway observed on Ni-Fe provided locally a higher activity for CO₂ hydrogenation. Overall, the importance of considering local gradients in catalytic reactors is demonstrated.

Introduction

The depletion of fossil energy sources and reduction of CO₂ emissions, with the aim to limit global warming, drive the need for new and efficient renewable energy systems. Currently available renewable power sources are mainly photovoltaics, wind- and water-power as well as biomass.^[1–2] The main challenge of renewable sources is their volatile availability.^[3] This leads to time-dependent fluctuations, which have to be balanced to maintain a stable electricity grid.^[4] Consequently, energy storage is necessary and plays a key role in the energy transition.^[2,4–5] One solution is to store electrical energy as chemicals with high energy density *e.g.* hydrogen, methane, other hydrocarbons or methanol.^[6] Methane is one of the most

promising candidates among the mentioned systems due to its broad application possibilities and an already existing transport infrastructure.^[7–8] It can be synthesized from CO₂ and (green) H₂ *via* the Sabatier reaction [Eq. (1)] using, most commonly, Ni-based catalysts.^[9–16]




Recently, promising bimetallic Ni-Fe-based catalysts gained broad attention as they offer enhanced catalytic activity and stability under stationary and fluctuating CO₂ methanation conditions.^[17–22] Hence, several studies have been conducted focusing on unraveling the promoting role of Fe. Various studies orient to the Ni:Fe ratio 3:1, proposed for CO methanation^[23–24] and also found active in CO₂ methanation.^[17–19,22,24–27] Notably, it was reported that the Ni-Fe alloy is structurally unstable during CO₂ methanation: Ni remains reduced while Fe is oxidized.^[19,21,28] By conducting extensive *ex situ* studies Burger *et al.*^[29] suggested a migration of Fe from the alloy to the particle surface. Thereby, Fe is (partly) oxidized to Fe²⁺. They assumed that this provides new redox sites for enhanced CO₂ activation.^[29] Complementary *operando* characterization including modulation excitation spectroscopy has recently confirmed this speculation.^[30] Highly dynamic FeO_x clusters were found to be formed on top of the Ni-Fe alloy particles under CO₂ methanation conditions. These FeO_x clusters exhibit a Fe⁰ ⇌ Fe²⁺ ⇌ Fe³⁺ redox behavior thereby providing active sites for enhanced CO₂ adsorption and dissociation. In addition, the FeO_x clusters protect and/or clean the Ni surface from oxygen impurities and thereby retain the active Ni⁰ sites for H₂ dissociation.^[20] DFT calculations further uncovered that CO₂ and H₂O show a very low tendency for oxidation of Ni


[a] M.-A. Serrer,⁺ M. Stehle,⁺ M. L. Schulte, Dr. E. Saraçi, Prof. J.-D. Grunwaldt
Institute for Chemical Technology and Polymer Chemistry (ITCP)
Karlsruhe Institute of Technology (KIT)
Engesserstr. 20
76131 Karlsruhe (Germany)
E-mail: grunwaldt@kit.edu

[b] M.-A. Serrer,⁺ M. L. Schulte, Dr. E. Saraçi, Prof. J.-D. Grunwaldt
Institute of Catalysis Research and Technology (IKFT)
Hermann-von-Helmholtz Platz 1
76344 Eggenstein-Leopoldshafen (Germany)

[c] H. Besser, Dr. W. Pfleging
Institute for Applied Materials – Applied Materials Physics (IAM-AWP)
Hermann-von-Helmholtz Platz 1
76344 Eggenstein-Leopoldshafen (Germany)

[⁺] These authors contributed equally to this manuscript.

 Supporting information for this article is available on the WWW under <https://doi.org/10.1002/cctc.202100490>

 © 2021 The Authors. ChemCatChem published by Wiley-VCH GmbH. This is an open access article under the terms of the Creative Commons Attribution License, which permits use, distribution and reproduction in any medium, provided the original work is properly cited.

atoms close to Fe, as Fe interacts more strongly with adsorbed oxygen (O^*).^[30] In contrast, medium tendency for oxidation of Fe by CO_2 and a high driving force for oxidation by H_2O was found.^[30] Thus, it seems that especially H_2O , which is formed by the reaction [Eq. (1)], has a strong effect on the structure of the bimetallic Ni–Fe catalyst.

However, the concentration of water changes along the reactor and this raises new questions regarding results obtained by the integral X-ray based *in situ* and *operando* studies, usually recorded at one fixed position of the catalyst bed.^[19,21,28] Apart from variation of the reactant and product concentration along the fixed-bed reactor, which may result in gradients in oxidation state and catalytic performance, gradients in temperature might occur due to the exothermic nature of the Sabatier reaction [cf. Eq. (1)]. Such gradients might influence the structural composition of the catalysts, particularly in case of the highly dynamic Ni–Fe system. Thus, it is crucial to reveal changes in activity, selectivity and catalyst structure along the reactor.^[31–32] This further allows to attribute parallel (side-)reactions, thermal degradation or poisoning to reaction zones within the catalyst bed.^[32–35]

Spatially-resolved activity data have recently been collected for various catalytic reactions, but mainly in coated channel reactors.^[36–37] For CO and CO_2 co-methanation,^[38] as well as CO_2 methanation^[39–40] activity profiles are reported for Ni-based catalysts on a coated plate reactor. However, CO_2 methanation is usually conducted in fixed-bed reactors on an industrial level.^[41] Plate reactors are limited to mimic industrially applied fixed-bed reactors, as flow properties and heat conductivity strongly differ with respect to different reactor types.^[39–41] In the last years, several technical approaches have been reported to enable reliable spatially-resolved experiments, even in fixed-bed reactors.^[41–44] Amongst these, setups based on an inserted capillary fixed at both ends with side-sampling hole(s) provided lowest intrusion and highest stability during profile acquisition.^[45–46]

In this work, we thus established a lab-scale setup for local activity profiling based on an inserted glass capillary with side-sampling orifices. First, axially resolved profiles of gas phase composition and temperature along a Ni/ γ - Al_2O_3 and a Ni–Fe/ γ - Al_2O_3 catalyst are recorded in fixed-bed geometry. The spatially-resolved profiles are further combined with structural analysis of the catalysts. In fact, the catalyst structure is investigated quasi-simultaneously at selected positions along a fixed-bed micro capillary reactor using quick X-ray absorption spectroscopy (quick XAS). Furthermore, diffuse reflectance infrared Fourier transform spectroscopy (DRIFTS) is used to gain insights into the presence of surface species. Overall, we aim at correlating the performance, temperature, and structure data to gain deeper insights into local relationships between structure and activity of the Ni- and Ni–Fe-based catalysts during CO_2 methanation.

Results and Discussion

Spatially-resolved experiments

To investigate the influence of structural catalyst composition on the catalytic activity, it is necessary to combine spatial concentration and temperature profiles in the reactor with structural information of the catalyst. For this purpose, we first recorded axially resolved temperature and concentration profiles in a newly built lab-scale testing setup (Figure 1a). This setup consisted of a motorized fixed-bed reactor enclosed by an oven unit. Inside the reactor, positioned in the longitudinal axis of the catalyst bed, a sampling capillary was mounted. The sampling capillary was fixed at both ends and had side-sampling orifices. A thermocouple was inserted into the capillary and its tip was aligned to the sampling orifices. To record spatial profiles, the whole oven/reactor unit was moved, while the capillary was kept in a fixed position. This allows to record several profiles without interruption and re-insertion of a new capillary.

In a second step, structural information was gained by performing spatially-resolved XAS studies. Different positions were probed along the model fixed-bed capillary reactor, *i.e.*, start (S), center (C) and end (E) position of the catalyst bed (cf. Figure 1b). To reduce recording and position adjustment times, quick XAS was applied. Further details are given in the experimental section. The results and derived correlations of structural catalyst composition and catalyst activity are discussed in the subsequent sections.

Spatially-resolved concentration and temperature profiles

First, we focused on recording temperature and concentration profiles of a monometallic 17 wt% Ni/ γ - Al_2O_3 and a bimetallic 17 wt% Ni_3_2Fe/γ - Al_2O_3 catalyst. Figure 2 shows the spatial profiles obtained during CO_2 methanation at 350 °C oven

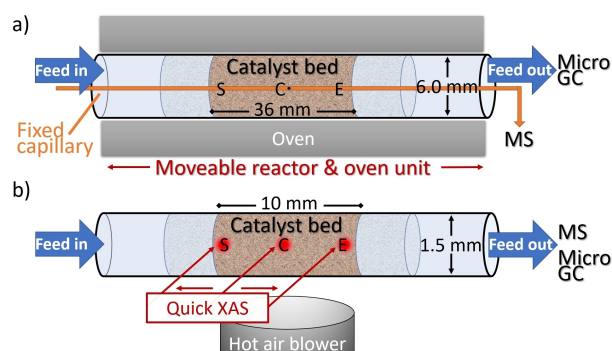


Figure 1. Scheme of the setups used for the spatially-resolved experiments. a) Newly built laboratory reactor including sampling capillary with inserted thermocouple. The capillary was fixed at both ends and exhibited side-sampling orifices. The oven/reactor unit can be moved along the fixed capillary to record profiles. b) Micro capillary reactor used for quick XAS experiments. The reactor was kept in a fixed position while the X-ray beam was alternatingly switched between start (S), center (C) and end (E) position to record structural data.

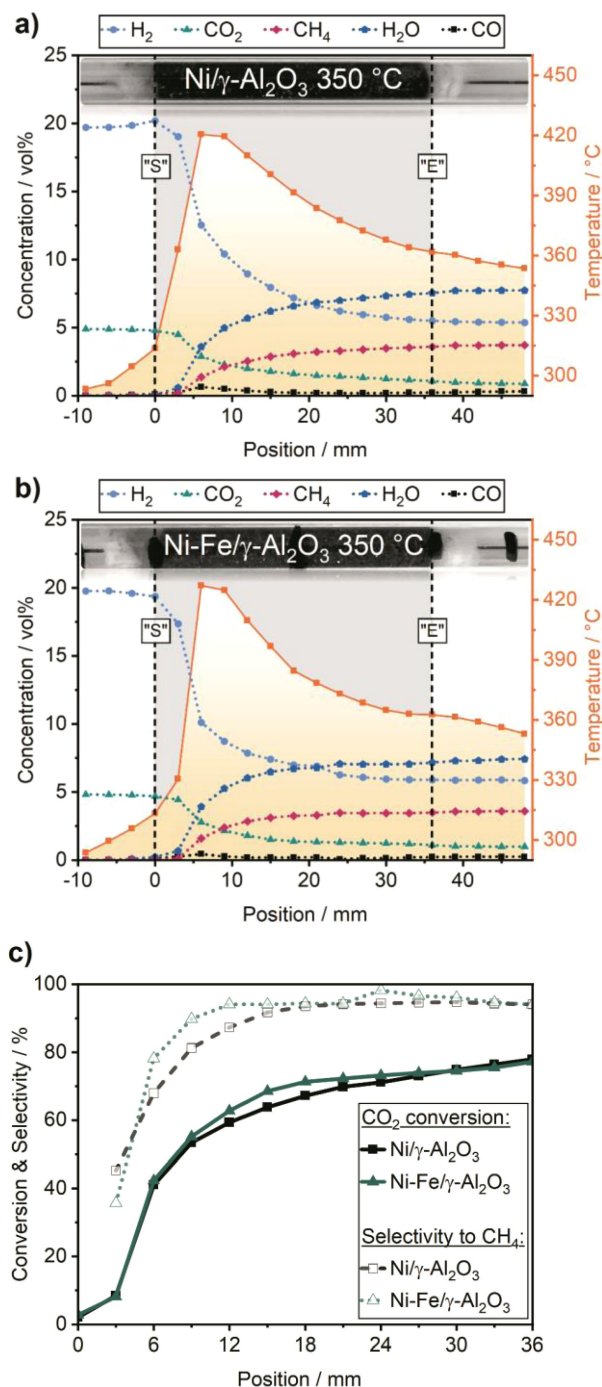
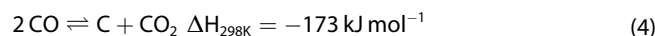
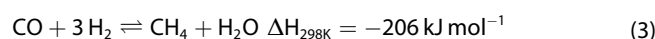
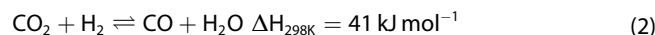


Figure 2. Temperature and concentration profiles during CO₂ methanation of the 17 wt% Ni/γ-Al₂O₃ catalyst (a) and the 17 wt% Ni_{3.2}Fe/γ-Al₂O₃ catalyst (b) obtained at 350 °C oven temperature at 1 atm and a total flow of 500 mL min⁻¹ (75% N₂, 20% H₂, 5% CO₂). The error was usually in the range of ±0.3 vol%. Comparison of spatially-resolved CO₂ conversion & selectivity profiles for both samples (c). The catalyst bed (250 mg catalyst (300–450 μm) diluted with 1.15 g SiC (210 μm)) ranged from position 0 mm to 36 mm.

temperature. The position at 0 mm marks the beginning (start, "S") of the catalyst bed and position 36 mm the end ("E"). The reactive gases were not pre-heated before entering the reactor. This led to a temperature difference of around 35 °C between oven setpoint and start of the catalyst bed (*cf.* Figure 2a and b).

A CO₂ conversion of 41% was achieved with the monometallic 17 wt% Ni/γ-Al₂O₃ catalyst within the first 6 mm of the catalyst bed (Figure 2c). This high catalytic activity was accompanied by formation of a hotspot of up to 420 °C (Figure 2a, position 6 mm). The temperature increase in correlation with the catalytic activity is due to the strong exothermic nature of the Sabatier reaction [*cf.* Eq. (1)]. Small amounts of CO were formed in this hotspot area as well, due to endothermic reverse water-gas-shift reaction (RWGS) [Eq. (2)].



In the center of the catalyst bed (18 mm), the temperature declined to 390 °C. This demonstrates a lower methanation activity compared to the start position (6 mm). Nevertheless, up to 67% of total CO₂ were already converted at this position. Notably, CO, which was formed at the start position of the catalyst bed, was found to be almost fully converted (Figure 2a). CO conversion might originate from hydrogenation to methane [Eq. (3)] or the Boudouard reaction under formation of C [Eq. (4)]. The formation of C depositions was already investigated by Mutz *et al.*^[47] applying Raman spectroscopy under similar reaction conditions as in this study. They have not observed any C formation, probably due to a high CO₂ concentration in the feed [*cf.* Eq. (4)]. Hence, it can be concluded that CO was fully converted to CH₄ in our case. Towards the end of the catalyst bed (36 mm) the temperature inside the reactor further decreased to 360 °C, while the total CO₂ conversion reached the final value of 78%.

Furthermore, the same experiment was conducted with the Ni_{3.2}Fe/γ-Al₂O₃ catalyst (Figure 2b) to investigate whether alternative mechanisms/kinetics exist upon addition of Fe. Gas composition, space velocity and temperature at the start of the catalyst bed were identical to the experiments conducted with the monometallic catalyst and equal initial conditions were achieved. The highest activity of the bimetallic Ni–Fe catalyst was observed within in the first 6 mm: CO₂ conversion reached 42% accompanied by an increase in temperature from 315 °C to 425 °C. In line with the monometallic Ni catalyst, the highest fraction of CO was found at this position most likely due to endothermic RWGS [*cf.* Eq. (2)].

At the axial center position of the catalyst bed (18 mm) the temperature declined to 385 °C due to decreasing catalytic activity (Figure 2b). A total CO₂ conversion of up to 71% was observed (Figure 2c). This was slightly higher than for the non-promoted Ni catalyst (67%). Further, previously formed CO was almost fully converted to CH₄ at this position. The observed trends continued throughout the end of the catalyst bed (36 mm): The temperature further decreased from 385 °C to 360 °C (Figure 2b) while CO₂ conversion slightly increased from 71% to 77% (Figure 2c).

Overall, the obtained reactor profiles unravel strong gradients in concentration and temperature during CO₂ metha-

nation in fixed-bed reactors. Furthermore, side reactions were observed at different spots along the catalyst bed. Addition of Fe enhanced the catalytic activity, especially within the first half of the catalyst bed. In addition, the structure of the catalysts might be subject to changes due to such gradients inside the catalyst bed. Hence, the influence of these gradients on the catalyst structure was investigated by spatially-resolved quick XAS and is discussed in the next section.

Spatial profiles of the oxidation states during CO₂ methanation

Quick XAS experiments were conducted to monitor structural changes along a fixed-bed micro reactor during CO₂ methanation. XAS spectra of both catalysts are shown in Figure 3. They were recorded in different states, *i.e.*, reduced state and under reaction conditions at the Ni and Fe K-edges at the start (S), center (C) and end (E) position (*cf.* Figure 1) of a fixed-bed micro capillary reactor (1 cm catalyst bed length). In Figure 3c one can see the differences in spectra for Fe. While Fe is reduced to the same extent at all three positions after TPR (linear combination analysis, LCA, *cf.* ESI), its oxidation state under reaction conditions is higher at the end of the catalyst bed. The relative fraction of species in the respective oxidation state derived by LCA is displayed in Figure 4.

The small amounts of Ni²⁺ observed at the start and center position (Figure 4, left) of the catalyst bed show that the monometallic Ni catalyst exhibited a high stability against oxidation during CO₂ methanation. The relative degree of oxidation was at all positions below 1.5% of the total Ni atoms and decreased slightly from the start towards the end. In the case of the bimetallic Ni–Fe catalyst (Figure 4, right) the Ni⁰ centers showed only slight oxidation, which is similar to the monometallic Ni catalyst (Figure 4, left). However, the relative amount of NiO was lower in the bimetallic Ni–Fe catalyst (*e.g.*, center: 0.7% vs. 1.4%). This confirms previous findings that Fe enhances the stability of active Ni⁰ centers under CO₂ methanation conditions.^[20]

A distinct Fe oxidation was observed at the start of the catalyst bed (Figure 4, right). The relative amount of Fe²⁺ increased from 13% to 33% to 38% in between start, center, and end position of the catalyst bed, respectively. Hence, a reverse trend of Fe and Ni oxidation along the catalyst bed was found. However, it should be noted that relative changes at the Ni K-edge were far less pronounced as at the Fe K-edge. Formation of FeO_x clusters was also recently observed during integral XAS measurements.^[30] In the mentioned publication, it was shown that these clusters are highly dynamic and enhance CO₂ activation.^[30] The spatially-resolved profiles now unravel that the amount of these crucial FeO_x species increases along the catalyst bed. To further investigate the origin of this oxidation, temperature-programmed oxidation (TPO) with CO₂ was conducted to unravel the oxidation potential of CO₂ on Ni and Fe.

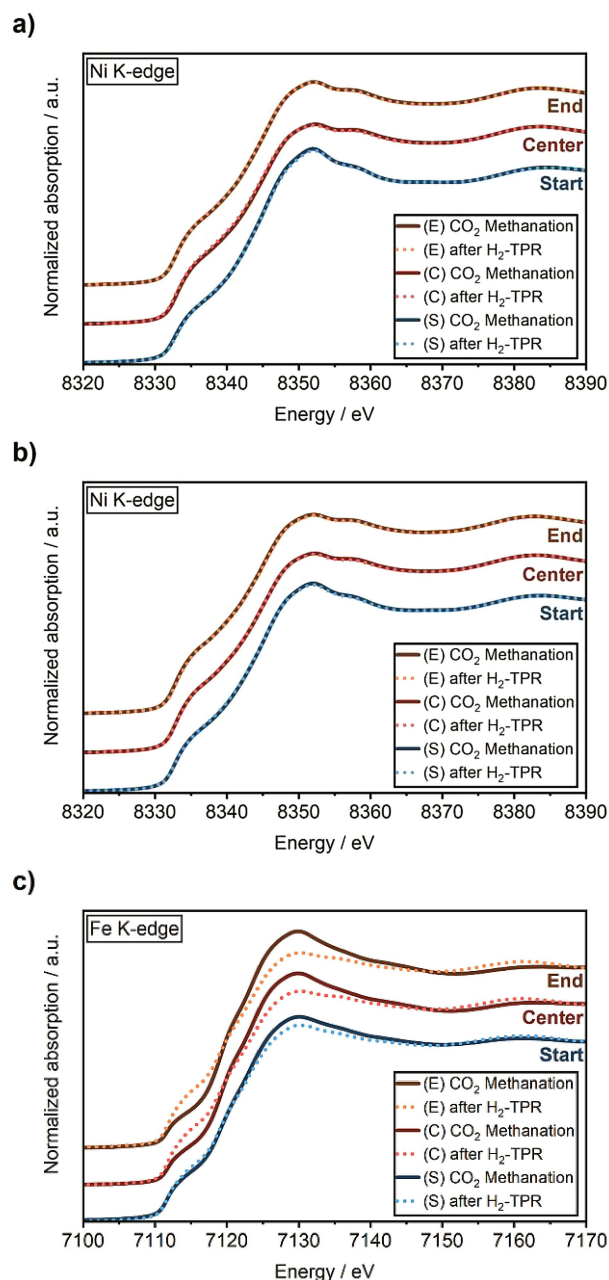


Figure 3. X-ray near edge absorption spectra (XANES) recorded at the Ni and Fe K-edges of the 17 wt% Ni/ γ -Al₂O₃ (a) and Ni_{3.2}Fe/ γ -Al₂O₃ (Ni K-edge (b); Fe K-edge (c)) catalyst after H₂-TPR (---) and during CO₂ methanation (—) at 350 °C (50 mL min⁻¹ 25 vol% H₂:CO₂ = 4:1 in N₂). The XANES spectra were recorded quasi-simultaneously with 4 Hz for 2 min at start (S), center (C) and end (E) position of the 1 cm catalyst bed in a micro capillary reactor.

Spatial profiles of CO₂ temperature programmed oxidation

The observed oxidation of Ni or Fe originates from oxygen containing species. Possible species in the CO₂ methanation are CO₂ or oxygen impurities.^[48–50] To investigate the oxidation potential of CO₂ in relation to temperature, we conducted a CO₂ TPO from 350 °C to 700 °C. First, the structural changes along the monometallic Ni catalyst bed were monitored at the Ni K-edge *via* quick XAS at the start (S), center (C) and end (E)

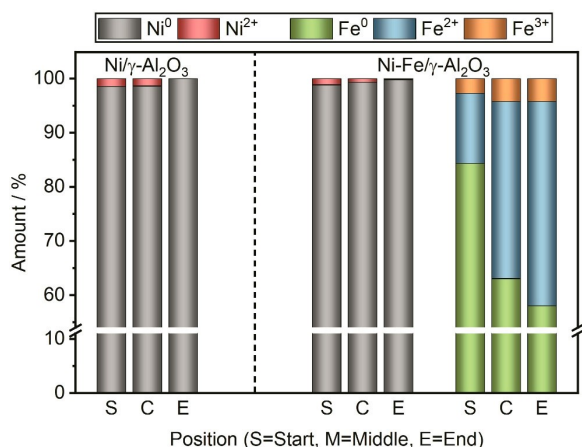


Figure 4. Relative changes of the oxidation states determined by linear combination analysis (LCA) of the XANES spectra recorded at the Ni and Fe K-edges of the 17 wt% Ni/ γ -Al₂O₃ (left) and Ni_{3.2}Fe/ γ -Al₂O₃ (right) catalyst during CO₂ methanation (50 mL min⁻¹ 25 vol% H₂:CO₂=4:1 in N₂) at 350 °C. The XAS spectra were recorded quasi-simultaneously with 4 Hz for 2 min at start (S), center (C) and end (E) position of the 1 cm catalyst bed in a micro capillary reactor.

position of the catalyst bed (Figure 5). To remove oxygen impurities in the gas feed, an oxygen trap was placed in front of the reactor and a small quantity of H₂ was kept in the dosed gas feed. The results in Figure 5 demonstrate that the monometallic Ni-based catalyst remained mainly reduced at all positions up to 450 °C in CO₂. Nevertheless, a slight oxidation of about 5.5% was noticed. Above 450 °C, a distinct increase in Ni²⁺ amount was observed at the center (C) and end (E) position of the catalyst bed (Figure 5). Thus, oxidation of Ni⁰ to Ni²⁺ becomes problematic above 450 °C. The lower degree of

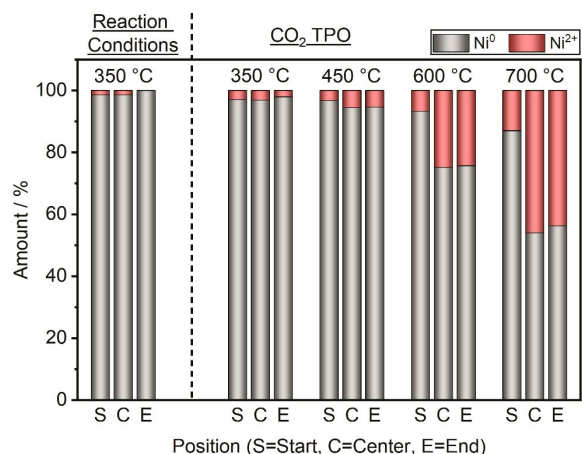


Figure 5. Relative changes of the oxidation states determined by linear combination analysis (LCA) of the XANES spectra recorded at the Ni K-edge of the 17 wt% Ni/ γ -Al₂O₃ catalyst during CO₂ methanation conditions ("Reaction Conditions": 50 mL min⁻¹ 25 vol% H₂:CO₂=4:1 in N₂) and TPO in an oxygen purified CO₂ feed ("CO₂ TPO": 5 mL min⁻¹ 300 ppm H₂ in CO₂) at various temperatures. The XAS spectra were recorded quasi-simultaneously with 4 Hz for 2 minutes at start (S), center (C) and end (E) position of the 1 cm catalyst bed in a micro capillary reactor.

oxidation at the start position was most likely due to the 300 ppm H₂ in the gas feed. However, these experiments provide evidence that CO₂ does not significantly contribute to the oxidation of Ni⁰ centers under commonly applied CO₂ methanation conditions (< 450 °C).

The same experiments were conducted with the bimetallic Ni–Fe catalyst (Figure 6). The results for the Ni K-edge were almost equivalent, but the degree of oxidation was always lower than for the monometallic Ni catalyst (*cf.* Figure 5). This is in line with findings that Fe provides a protective role on Ni⁰ centers.^[20,51]

LCA results obtained at the Fe K-edge are given in Figure 6b. The calcined and reduced catalyst and a FeO pellet were used as references (*cf.* experimental section). At the start position it was found that the amount of Fe⁰ decreased from 84% to 62% while Fe²⁺ and Fe³⁺ increased from 13% to 26% and 3% to 12%, respectively compared to reaction conditions.

The same trends, but less pronounced, were observed at the center (C) and end (E) position. The amount of Fe⁰ in the center changed from 63% to 47%, Fe²⁺ from 33% to 41%, and

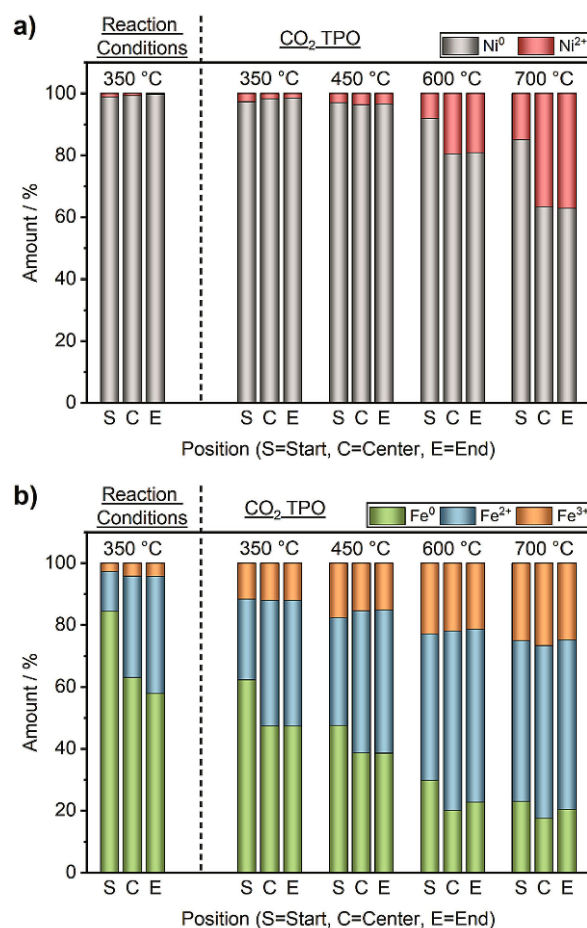


Figure 6. Relative changes of the oxidation states determined by linear combination analysis (LCA) of the XANES spectra recorded at the Ni (a) and Fe (b) K-edges of the 17 wt% Ni_{3.2}Fe/ γ -Al₂O₃ catalyst during CO₂ methanation ("Reaction Conditions": 50 mL min⁻¹ 25 vol% H₂:CO₂=4:1 in N₂) and during TPO in an oxygen purified CO₂ feed ("CO₂ TPO": 5 mL min⁻¹ 300 ppm H₂ in CO₂) at various temperatures. The XAS spectra were recorded quasi-simultaneously with 4 Hz for 2 minutes at start (S), center (C) and end (E) position of the 1 cm catalyst bed in a micro capillary reactor.

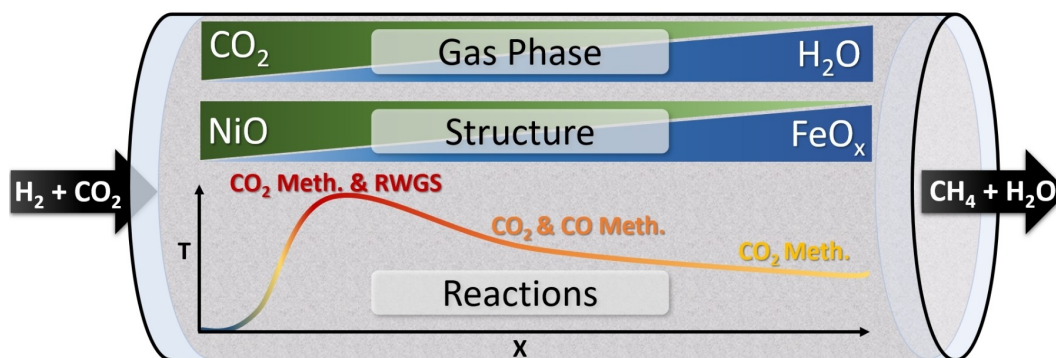


Figure 7. Overview on the trends observed in the spatially-resolved studies conducted in fixed-bed reactors with a 17 wt% Ni/ γ - Al_2O_3 catalyst and a 17 wt% $\text{Ni}_{3/2}\text{Fe}/\gamma$ - Al_2O_3 catalyst during CO_2 methanation ($\text{H}_2:\text{CO}_2=4:1$) performed at 1 atm and an oven setpoint temperature of 350 °C.

Fe^{3+} from 4% to 12%. At the end of the catalyst bed, the amount of Fe^0 declined from 58% to 47% while the amount of Fe^{2+} increased from 38% to 41% and Fe^{3+} from 4% to 12%. With increasing temperature, a decreasing Fe^0 amount was observed at all positions. At 600 °C the Fe^0 fraction reduced to 30% at start, 20% center and 23% end position. This provides evidence that Fe gets oxidized by CO_2 with respect to CO_2 partial pressure and temperature. Hence, we can conclude that either FeO_x species clean the Ni surface from oxygen, or that dissociative CO_2 activation occurs at the FeO_x centers. By this, surface oxygen species are formed and subsequently bound into the FeO_x phase. Both explanations are in line with the lower degree of Ni oxidation during CO_2 TPO upon addition of Fe. Switching from CO_2 methanation to CO_2 TPO conditions immediately led to formation of higher amounts of FeO_x . This uncovers that H_2 dynamically reduces some FeO_x species during CO_2 methanation. Upon removal of H_2 in the feed, distinct formation of Fe^{3+} species from around 4% to 12% was observed. Hence, it can be concluded that H_2 mainly prevents formation of Fe^{3+} species.

Correlation of local gas composition and catalytic activity with structural properties of the methanation catalysts

Strong gradients in temperature and concentration profiles occur over the catalyst bed in a fixed-bed reactor during CO_2 methanation. These gradients are connected to distinct structural changes of the catalyst along the axial direction of the reactor. Figure 7 summarizes schematically the most important trends and findings described in the previous sections.

First, a monometallic 17 wt% Ni/ γ - Al_2O_3 catalyst was investigated. The highest gradients in CO_2 concentration, conversion, catalytic activity, and temperature were found in the first part of the reactor. The fraction of oxidized Ni species was highest at the start position and declined along the catalyst bed. Nevertheless, the fraction of Ni that was in oxidized state was only 1.5%. Hence, this oxidation probably occurs predominantly on the surface of the Ni particles, as low coordinated Ni atoms are more prone to oxidation.^[50,52] The formation of surface oxygen species indicate

that dissociative CO_2 activation occurs, leading to formation of CO^* and O^* , as speculated also by Vogt *et al.*^[50]

In order to gain additional insight into surface species within this first reaction zone, we conducted DRIFTS studies under standard CO_2 methanation conditions on the 17 wt% Ni/ γ - Al_2O_3 catalyst (Figure 8, grey). The reaction mechanism of the CO_2 methanation strongly depends on the catalyst system and is, due to its complexity, still under discussion.^[8,49,53] In general, it can be divided into two pathways: The “hydrogen assisted” pathway describes the direct adsorption and hydrogenation of CO_2 via formate species as intermediates.^[13,54–57] The “dissociative” pathway depicts the dissociative adsorption of CO_2 under formation of CO as intermediate species.^[48,58] CO is then either directly hydrogenated to CH_4 or via formation of surface carbon species. After H_2 -TPR, the catalyst surface was clean from any species at 250 °C (Figure 8, bottom). After switching to CO_2 methanation conditions at 250 °C (Figure 8, middle), we observed bands of two possible intermediates, namely adsorbed CO and formate. The band at around 1930 cm^{-1} originates from stretching vibrations of bridged carbonyl species.^[28,59–61] The band at around 2040 cm^{-1} represents

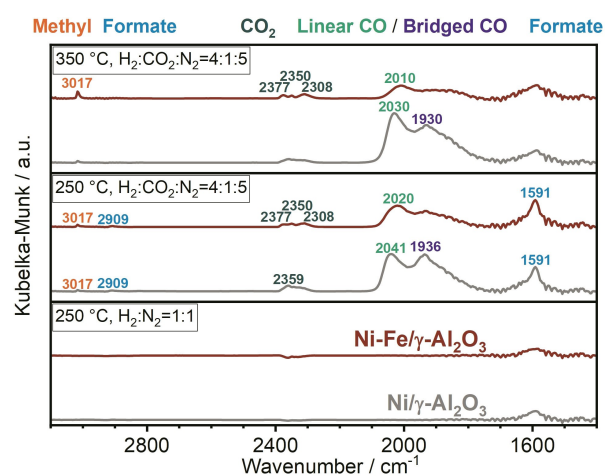


Figure 8. DRIFTS spectra of the 17 wt% Ni/ γ - Al_2O_3 (grey) and the 17 wt% $\text{Ni}_{3/2}\text{Fe}/\gamma$ - Al_2O_3 (brown) catalyst (100–200 μm) at 250 °C and 350 °C under reducing and CO_2 methanation conditions with a total flow of 115 mL min^{-1} .

terminally CO adsorbed atop a single Ni atom.^[28] Formate bands appear around 1590 cm^{-1} and 2909 cm^{-1} .^[15,50,62] Bands in the region from around $2280\text{--}2400\text{ cm}^{-1}$ can be assigned to CO_2 .^[58,62] C–H stretching vibrations of the desired product CH_4 are allocated to around 3016 cm^{-1} .^[15,62] Hence, we can conclude that both CO_2 activation mechanisms, the associative and dissociative pathway, take place.

Upon increasing the temperature from $250\text{ }^\circ\text{C}$ to $350\text{ }^\circ\text{C}$, CO_2 methanation was initiated (Figure 8, top) and intermediate species are converted to CH_4 . Thus, declining band intensities depict conversion of intermediate species. This was the case for the formate bands at 1590 cm^{-1} , which was hardly visible at $350\text{ }^\circ\text{C}$. Hence, formate is one of the main intermediate species on Ni-based systems. The band intensity for bridged carbonyl species at 1933 cm^{-1} remained unchanged, while the band intensity of terminally adsorbed CO at around 2030 cm^{-1} increased. This shows that at elevated temperature either CO_2 dissociation is enhanced or that formate is converted under formation of linear CO species. However, an increasing amount of CO surface species on the Ni surface is to be seen rather problematic, as CO tends to poison active Ni^0 centers.^[50] The shift of the CO bands from 2041 cm^{-1} at $250\text{ }^\circ\text{C}$ to 2030 cm^{-1} at $350\text{ }^\circ\text{C}$ indicates an oxidation of surface Ni^0 to NiO .^[59–61] This is in line with the results obtained during our XAS studies.

With our spatially-resolved experiments, we unraveled that this oxidation of Ni centers occurs in moderate to high activity zones, *i.e.*, start and center (*cf.* Figure 7). Hence, we conclude that oxidation of surface Ni^0 centers occurs due to dissociative CO_2 activation under formation of O^* and (mainly linear adsorbed) CO^* . Nevertheless, the CO_2 TPO experiment revealed that Ni oxidation is self-limiting. This is probably due to surface blocking by CO and O after some time. The increased amount of oxidized Ni species after removal of H_2 of the feed (CO_2 TPO) shows that H_2 is crucial to dynamically free some Ni centers from oxygen adsorbents. Notably, CO formation was only observed in the hotspot area during our spatially-resolved studies. Hence, gaseous CO is either formed from RWGS reaction [*cf.* Eq. (2)] or from a fast CO_2 dissociation but hindered CO conversion. In the other parts of the reactor, CO was quickly converted into CH_4 . This confirms previous findings that CO methanation proceeds faster than CO_2 methanation.^[63]

The same experiments were conducted with the bimetallic 17 wt% $\text{Ni}_{3.2}\text{Fe}/\gamma\text{-Al}_2\text{O}_3$ catalyst. Almost identical concentration and temperature profiles were obtained for Ni-Fe as compared to Ni (*cf.* Figure 7). However, a hindered oxidation of Ni in the presence of Fe was observed. This might either be due to a protective mechanism of $\text{Fe}^{[20]}$ or due to substitution of Ni surface atoms with $\text{Fe}(\text{O}_x)$ species.

DRIFTS experiments (Figure 8) showed a formate band (1590 cm^{-1}) with the same intensity at $250\text{ }^\circ\text{C}$ for both catalyst systems. Hence, Fe does not promote associative CO_2 activation under formation of formate species. This shows that associative CO_2 activation occurs either on Ni or the $\gamma\text{-Al}_2\text{O}_3$ support. As the lower amount of surface Ni in the bimetallic system did not result in lower formate bands, it can be assumed that associative CO_2 activation occurs mainly on $\gamma\text{-Al}_2\text{O}_3$, which is in line with other reports.^[13,54–57,64]

However, distinct differences in adsorbed CO species were found in the case of the bimetallic Ni–Fe catalyst (Figure 8, brown): The intensity of all CO bands was visibly lower as compared to the monometallic Ni catalyst (Figure 8, grey). This provides evidence that Fe either prevents CO adsorption or its formation. The first might be due to alteration of the electronic properties of Ni, the latter could be assigned to enhanced CO dissociation. Such an enhanced CO dissociation is in line with theoretical DFT calculations.^[23] The shift of the band of terminally adsorbed CO (from 2011 cm^{-1} to 2023 cm^{-1}) was, as discussed before for Ni, also observed for the Ni-Fe catalyst but not as pronounced. This indicates a lower surface oxidation of the Ni atoms upon addition of Fe, which is in line with the findings from our XAS experiments, as well as previous studies in which a protective role of Fe was reported.^[20]

Both effects due to Fe promotion, *i.e.*, increased CO dissociation and prevention of active Ni^0 sites, can be attributed to the formation of highly dynamic $\text{Fe}(\text{O}_x)$ clusters on top of the catalyst particles as shown in our previous study.^[30] In detail, the results indicate that CO_2 adsorbs preferably on $\text{Fe}(\text{O}_x)$ clusters. Further, these clusters provide a highly dynamic redox behavior which promotes the dissociative CO_2 activation mechanism and keeps the active Ni centers clean from adsorbed CO_2 or CO. By this, the active Ni^0 centers in bimetallic Ni–Fe catalysts are preserved for H_2 dissociation.^[30] In fact, a slightly higher temperature and CO_2 conversion was noticed at the start position of the catalyst bed for the Ni–Fe catalyst (*cf.* Figure 2b and c). This confirms the more efficient CO_2 activation in presence of such $\text{Fe}(\text{O}_x)$ clusters.^[30]

Our spatially-resolved experiments now show that the amount of these FeO_x species increases along the catalyst bed. This is interesting, as the concentration of CO_2 , which is the only oxygen source in the gas feed, declines along the catalyst bed (*cf.* Figure 7). Thus, one of the (by-)products formed during CO_2 methanation is probably the driving force for Fe oxidation, although CO_2 TPO experiments (*cf.* Figure 6b) confirmed a slight oxidizing potential of CO_2 on Fe. The only other species which contains oxygen and exhibits an increasing amount along the catalyst bed is H_2O . In fact, a correlation of the water concentration with the degree of oxidation of Fe was found (*cf.* Figure 7). Similar findings were reported based on *ex situ* studies with reduced Fe in CO_2 and $\text{CO}_2/\text{H}_2\text{O}$ containing feeds.^[65] Further, DFT studies uncovered that H_2O and not CO_2 is the driving force for oxidation of Fe in bimetallic Ni–Fe catalysts during CO_2 methanation whereas metallic Ni seems to be stable in the presence of water. Nevertheless, based on XPS and NEXAFS studies, Giorgianni *et al.*^[21] reported that a hydroxylation of Ni by H_2O can occur while they found that Fe^{2+} can be added to prevent Ni hydroxylation and to promote CO_2 activation. The spatial profiles in this study showed that Ni was in its most reduced state at the end of the catalyst bed, where the highest amount of H_2O was found (*cf.* Figure 7). This trend was observed for both catalysts in our study, and we did not find any hints for hydroxylation of Ni in the spatially resolved XANES spectra. Our findings are supported by recent DFT studies^[30] suggesting that the main driver for oxidation of Ni is CO_2 dissociation while for Fe it is H_2O . The contradicting results obtained for Ni as compared to the XPS and NEXAFS

study^[21] might be due to the low pressure that has to be applied during such experiments. This further highlights the importance of conducting experiments as close as possible to realistic reaction conditions.

Conclusions

Local activity and structure profiling was conducted for Ni-based CO₂ methanation catalysts with the aim to investigate changes in the catalyst structure with respect to catalytic activity and local composition of the gas phase. First, gradients in gas phase composition and temperature along a monometallic 17 wt% Ni/ γ -Al₂O₃ and a bimetallic 17 wt% Ni_{3,2}Fe/ γ -Al₂O₃ catalyst were resolved by local activity profiling using a fixed-bed reactor setup. By combining the obtained reactor profiles with spatially-resolved quick XAS experiments conducted in a micro capillary fixed-bed reactor, we were able to reveal the influence of gradients in gas phase on the structure of both Ni-based CO₂ methanation catalysts.

The highest gradients were observed in the first third of the reactor where both catalysts exhibited a very high methanation activity of around 50% CO₂ conversion. This resulted in the formation of a pronounced hotspot and led to local CO formation by RWGS reaction. However, this CO formation was not found to be problematic in terms of integral selectivity, as CO was quickly hydrogenated to CH₄ downstream of the catalyst bed.

The highest degree of oxidation of Ni was observed at the hotspot position. Nevertheless, XAS and DRIFTS studies indicated that mainly surface Ni atoms were prone to oxidation. Based on DRIFTS studies and earlier work in literature, we conclude that dissociative CO₂ activation on Ni⁰ leads to formation of CO* and O*. The DRIFTS studies further showed that linear and bridged CO* is strongly bound to the Ni surface in the case of the monometallic 17 wt% Ni/ γ -Al₂O₃ catalyst. Furthermore, a direct correlation of the fraction of oxidized Ni with the concentration of CO₂ was found, indicating that CO* and O* from CO₂ dissociation cause blocking and oxidation of Ni⁰ surface atoms. As these surface species were predominantly observed in the hotspot, it can be concluded that especially in this area the active Ni⁰ centers at the surface need to be kept free from CO and protected from oxidation.

Identical experiments conducted with the bimetallic 17 wt% Ni_{3,2}Fe/ γ -Al₂O₃ catalyst unraveled an alternative reaction pathway, as CO₂ is adsorbed and dissociated on Fe centers. Subsequently, the formed O* is bound under formation of FeO_x. Hence, the addition of Fe leads to a lower fraction of oxidized Ni. The total degree of oxidation of Fe increased towards the end of the catalyst bed, in correlation to a rising amount of H₂O and a declining amount of H₂, CO, and CO₂ in the gas atmosphere. Hence, the oxidation of Fe is more sensitive to the concentration of H₂O in the gas atmosphere rather than to CO₂. This is in contrast to the oxidation of Ni. In summary, reaction-induced changes in gas composition directly and strongly influence the structural composition of Fe.

Furthermore, DRIFTS experiments indicate that the presence of Fe hinders binding of CO species to the catalyst surface. In

comparison to the monometallic Ni catalyst, the presence of Fe led to a decreased intensity of CO bands and an increased methyl band intensity during CO₂ methanation. Thus, it can be concluded that Fe on the one hand protects active Ni⁰ species and on the other hand not only hampers formation of CO surface species, but even promotes their hydrogenation to CH₄. Our spatially-resolved studies showed that this effect is crucial especially in the hotspot area (highest activity), where highest amounts of CO are formed due to RWGS reaction. CO₂ conversion as well as selectivity to CH₄ were found to be distinctly higher for the Ni–Fe catalyst compared to the monometallic Ni catalyst.

Overall, the spatially-resolved results presented in this study uncover the local dependency of structural properties of the catalysts on reaction-induced changes in gas phase composition of Ni-based CO₂ methanation catalysts in fixed-bed reactors. Hence, the here performed investigations revealing the gradients in gas phase composition, temperature, and catalyst structure represent an important step forward for fundamental catalyst understanding. In future, the studies should be further deepened by reactor simulations aiming at an optimization of industrial fixed-bed reactors for CO₂ methanation.

Experimental Section

Catalyst preparation, catalytic tests and product analysis

A 17 wt% Ni/ γ -Al₂O₃ and 17 wt% Ni_{3,2}Fe/ γ -Al₂O₃ catalyst were prepared by homogeneous precipitation with urea over 18 h at 96 °C. The solids were filtered, washed with 500 mL deionized water, dried overnight at 110 °C and calcined for 4 h at 500 °C (5 °C min⁻¹) in static air. Preparation details are given in refs.^[20,66] The catalyst powder was pressed into a pellet (5 tons), crushed, and sieved into fractions of 100–200 μ m and 300–450 μ m. The specific surface areas were determined by N₂-physisorption measurements. The specific surface area amounted to \sim 200 m²g⁻¹ for γ -Al₂O₃ and for both Ni-based catalysts to around 220 m²g⁻¹.^[66] Experimental details of the N₂-physisorption experiments along with further catalyst characterization results can be found in ref.^[66]

Catalytic tests of the 17 wt% Ni/ γ -Al₂O₃ and 17 wt% Ni_{3,2}Fe/ γ -Al₂O₃ have been conducted in a newly established lab-scale testing setup (c.f. Figure 9). This setup allows to simultaneously record, in addition to the quantitative integral catalytic activity (via gas chromatography), spatially-resolved concentration (via mass spectrometry) and temperature profiles (via thermocouple) in a single run. Furthermore, by using a sampling capillary which was fixed at both ends, profile acquisition can be repeated or performed under different reaction conditions (e.g., oven temperature).

The reactor (Figure 9, left) is based on a plug flow quartz glass reactor (length 33 cm, outer diameter 10 mm, inner diameter 6 mm). The catalyst was adjusted to a sieve fraction of 300–450 μ m and the catalyst bed in the quartz glass reactor was diluted 1:4 in SiC (210 μ m) to reduce formation of a hotspot. The exact amounts of the used catalysts and inert material are given in Table 1.

The packed catalyst bed was fixed in the quartz glass reactor with quartz glass wool resulting in a bed length of 36–39 mm. To measure the concentration and temperature profiles along the catalyst bed, a glass capillary (length 60 cm, outer diameter 450 μ m, inner diameter 320 μ m, Polymicro Technologies) was

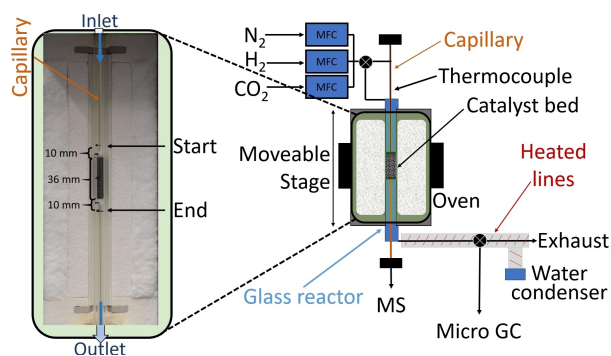


Figure 9. (Left) Vertical plug flow quartz glass reactor with a 36 mm long catalyst bed mounted inside the oven unit. Start and end position mark the measurement range. (Right) Scheme of the experimental setup including gas-dosing (mass flow controllers, "MFC") and moveable stage to conduct spatially-resolved activity measurements along the catalyst bed during CO₂ methanation.

Catalyst	m _{cat} [g]	m _{SiC} [g]
17 wt % Ni/γ-Al ₂ O ₃	0.2509	0.9698
17 wt % Ni _{3.2} Fe/γ-Al ₂ O ₃	0.2513	0.9656

placed in the center of the reactor. Gas sampling along the catalyst bed was enabled by 2 pairs of holes in the capillary (opposing holes, 90° offset between two different pairs, 500 μm distance) with a diameter of about 50 μm. In order to avoid crack formation or material modification, the holes were drilled using an ultrafast fiber laser (Tangerine, Amplitude Systèmes, France) with a pulse length of 400 fs, a laser wavelength of 1030 nm, and an average laser power of 4.5 W. The temperature inside the catalyst bed was simultaneously recorded by a thermocouple (type K, 400 mm length, diameter 150 μm), which was inserted into the capillary and tip aligned between the sampling hole pairs. The capillary was fixed while the reactor and the oven (length 27 cm) were moved by a motorized linear stage (Zaber, travel range 100 mm, accuracy 25 μm, repeatability < 2 μm), as depicted in Figure 9, right. The junction between sampling capillary and reactor was made by graphite ferrules (VICI). This allowed gas-tight operation while the reactor could still be moved along the capillary. Heating of the sampling capillary outside the reactor was realized by a hot air blower to prevent water condensation. Gas composition and flow were adjusted using mass flow controllers (Bronkhorst), quantitative gas analysis was performed using a micro GC (Agilent 490) with N₂ as internal standard. The conversion and selectivity were calculated as described in ref.^[20] To prevent the condensation of water in the product feed, the outlet lines were heated to 150 °C.

Prior to the experiments, the catalysts were activated by H₂ TPR for 2 h at 500 °C (10 °C min⁻¹) in 55 vol % H₂:N₂. Subsequently, the reactor was cooled down to the reaction temperature and the gas feed was switched to CO₂ methanation conditions of 25 % H₂:CO₂ = 4:1 in N₂ (Table 2).

After reaching a steady state, the spatially-resolved measurements were performed at positions between 10 mm in front and 10 mm behind the catalyst bed (Figure 9) in 3 mm steps for 15 min each. After a waiting time of 5 min, the ion currents and temperature data were averaged over 10 min to obtain the value for the respective position. Hence, the acquisition of a combined concentration and temperature

Table 2. Gas flows for spatially-resolved measurements during CO₂ methanation in the laboratory reactor.

	N ₂ [mL min ⁻¹]	H ₂ [mL min ⁻¹]	CO ₂ [mL min ⁻¹]
<i>In situ</i> reduction	165	200	–
CO ₂ methanation	375	100	25

profile took about 5 h. The profiles were recorded at 350 °C (oven setpoint temperature). Additionally, temperature profiles were recorded in 500 mL min⁻¹ N₂ along the spent catalyst bed as well as in an empty reactor without gas flow (1 mm steps, 30 s each). The gas concentrations were calculated based on the profiles of the ion currents measured by the mass spectrometer (MS). An overview on the potential fragmentation in the MS of each species during the experiments is shown in Table 3.^[67]

Due to strong variations in the gas feed composition, the internal pressure in the MS was instable, leading to fluctuations in the ion currents. Hence, the measured ion currents were normalized [Eq. (5)] to the fragment 14 of N₂ after subtracting the contribution of CH₄ (cf. Table 3).

$$N_{MS} = \frac{14^{in}}{14^{out} - \left(\frac{20.4}{88.75}\right) 15^{out}} = \frac{N_2^{in}}{N_2^{out}} \quad (5)$$

Ion currents were converted to vol% by applying a linear correlation between MS signals (Fragments: H₂=2; CH₄=15; CO₂=44) and gas concentrations determined by the micro GC (inlet = bypass; outlet = integral performance) according to Equation (6).

$$N_{GC} = \frac{N_2^{in}}{N_2^{out}} \quad (6)$$

The concentration of CO was calculated *via* the carbon balance as no other carbon containing by-products were observed by the micro GC. The concentration of H₂O, which was not quantified by the micro GC, was calculated *via* the stoichiometry of the Sabatier reaction [Eq. (1)].

Spatially-resolved quick XAS profiles

Structural studies were conducted in a separate experiment, also with a fixed-bed of the sieved catalyst and on-line analysis with a MS and a micro GC (Figure 1). The used setup consisted of a micro quartz capillary reactor (1.5 mm diameter, 20 μm wall thickness, 1 cm catalyst bed length, 100–200 μm catalyst sieve fraction, Hilgenberg GmbH) heated by a hot air blower (Oxford GSB-1300).^[68] The 17 wt % Ni/γ-Al₂O₃ and 17 wt % Ni_{3.2}Fe/γ-Al₂O₃ catalysts were diluted 1:1.3 with γ-Al₂O₃ to obtain an optimized absorption step. Spatially-resolved XAS studies were conducted at the SuperXAS

Table 3. Fragment distribution in the mass spectrometric data of selected species present during the spatially-resolved measurements for the methanation of CO₂.^[67]

m/z	2	14	15	18	28	44
H ₂	100%	–	–	–	–	–
CO ₂	–	–	–	–	10%	100%
CO	–	–	–	–	100%	–
CH ₄	–	20%	89%	–	–	–
H ₂ O	–	–	–	100%	–	–
N ₂	–	14%	–	–	100%	–

beamline at the Swiss Light Source (SLS)^[69], Paul Scherrer Institute (PSI) using quick scanning EXAFS (quick XAS)^[70] mode. To obtain one XAS spectrum, Ni and Fe K-edge were recorded simultaneously for 2 min in transmission mode at start, center and end position of the catalyst bed, respectively. Subsequently, the spectra obtained with a Si(111) channel-cut crystal scanning at 4 Hz were averaged using a MatLab script.

Both catalysts were activated by H₂-TPR in 20 mL min⁻¹ 50% H₂:N₂, 2 h at 500 °C (10 °C min⁻¹) and 1 bar. Subsequently, the samples were cooled down to room temperature to record XAS spectra of the reduced catalyst state. After the acquisition at room temperature, the catalysts were heated to 350 °C under reducing conditions. Subsequently, the reaction was initiated by switching to methanation conditions (50 mL min⁻¹ 25 vol% H₂:CO₂=4:1 in N₂) in order to verify the catalytic activity. The aim was to conduct the experiment under reaction conditions as similar as possible to the experiments performed in the laboratory fixed-bed reactor for spatial profiling. However, due to restrictions of the model reactor that was required to conduct X-ray absorption experiments, harsher conditions were present in this case: WHSV ≈ 120 L g_{cat}⁻¹ h⁻¹ (laboratory reactor) vs. ≈ 2000 L g_{cat}⁻¹ h⁻¹ (micro capillary), r(CH₄) ≈ 175 mmol g_{cat}⁻¹ h⁻¹ (laboratory reactor) vs. ≈ 850 mmol g_{cat}⁻¹ h⁻¹ (micro capillary); S(CH₄) ≈ 100% (laboratory reactor) vs. ≈ 80% (micro capillary). In addition, the laboratory reactor and the micro quartz capillary reactor might provide different heat conductivity and thus different heat transport properties.^[71] Hence, results obtained in this model reactor should be mainly considered to depict trends occurring inside the laboratory fixed-bed reactor and careful reactor simulations^[72] are needed to directly transfer the results.

To investigate whether CO₂ has an impact on oxidation of Ni-based catalyst systems and at which temperature this becomes problematic, a temperature-programmed oxidation by CO₂ ("CO₂ TPO") was performed using a gas feed consisting of 5 mL min⁻¹ 300 ppm H₂ in CO₂. XAS spectra were recorded at 350 °C, 450 °C, 600 °C and 700 °C at the start, middle and end position of the catalyst bed, respectively. Hence, structural profiles along the catalyst bed were obtained for different temperatures.

The recorded spectra were energy calibrated to a simultaneously measured Ni metal foil, normalized and exported as μ(E) vs. E files using the "ProXAS-GUI" software (version 2.9) by Adam Hugh Clark.^[73] As the Ni and Fe K-edge spectra were recorded in one scan, each data file obtained from the bimetallic catalyst was cut in two after calibration and normalization. The normalized and averaged XANES spectra were analyzed by the linear combination analysis (LCA) module of Athena^[74] in the energy interval from -30 eV to +50 eV using the spectrum of the fully oxidized sample after calcination at 500 °C in air and the spectrum of the reduced sample after H₂-TPR at the Ni and Fe K-edge. Additionally, a FeO reference was measured for LCA at the Fe K-edge.

Diffuse reflectance Fourier transform infrared spectroscopy

Diffuse reflectance Fourier transform infrared spectroscopy (DRIFTS) measurements were performed on a commercial Bruker Vertex 70 FT-IR spectrometer with a Hg-Cd-Te (MCT) detector (cooled by liquid nitrogen). A Harrick Praying Mantis™ high temperature reaction cell with a flat CaF₂ window was used. The cylindrical 4 × 6 mm (h × w) sample chamber was filled with ~60 mg catalyst (100–200 μm). The temperature was controlled using an ImageIR® 8300 camera in "through-glass" mode.

Gas compositions were adjusted *via* mass flow controllers (Brooks Instruments) calibrated by a Mesalabs Bios DryCal definer 220 gas flow calibrator. An Agilent 490 micro GC (Channel 1: 10 m PorAPLOT

Q, 0.25 mm diameter, carrier gas helium; Channel 2: 10 m mole sieve column with 5 Å, 0.25 mm diameter, carrier gas argon) was used to analyze the outlet gases.

The 17 wt% Ni/γ-Al₂O₃ and 17 wt% Ni_{3.2}Fe/γ-Al₂O₃ catalysts were investigated under various gas compositions and temperatures. A total gas flow of 115 mL min⁻¹ was used in all experiments. Prior to the DRIFTS studies, the catalysts were pre-reduced for 2 h at 500 °C in 50% H₂/N₂ in an external device. In addition, the surface of the pre-reduced catalysts was cleaned at approximately 400–450 °C (controlled with IR Camera) over 2 h at N₂:H₂=1:1 in the Harrick Praying Mantis™ high temperature reaction cell. Subsequently, background corrected (CaF₂, 100 μm) DRIFTS spectra were recorded (4 cm⁻¹ resolution, 200 scans) at 250 °C and 350 °C under CO₂ methanation conditions (H₂:CO₂:N₂=4:1:5).

Acknowledgements

The authors would like to thank the X10DA (SuperXAS) beamline, Dr. Maarten Nachtegaal (PSI), Dr. Olga Safonova (PSI) and Dr. Adam Hugh Clark (PSI) at the Swiss Light Source (SLS) in Villigen (Switzerland) for providing beam time and support during experiments and raw data treatment. Further, we gratefully acknowledge Dr. Henning Lichtenberg, Charlotte Fritsch and Florian Maurer for beamtime support. The German Federal Ministry of Education and Research (BMBF) is gratefully acknowledged for financial support within the Kopernikus Project P2X and, further, we thank the SPP2080 (DFG-priority program, GR 3987/13-1 and 14-1) both for financial support and a discussion forum for "Catalysts and reactors under dynamic conditions for energy storage and conversion". We acknowledge the Helmholtz Research Program STN for financial support related to laser drilling of the glass capillaries. Open access funding enabled and organized by Projekt DEAL.

Conflict of Interest

The authors declare no conflict of interest.

Keywords: Spatially-resolved *operando* study · Carbon dioxide hydrogenation · Concentration and Temperature Profiles · Nickel-Iron Methanation Catalyst

- [1] R. Scholz, M. Beckmann, C. Pieper, M. Muster, R. Weber, *Renewable Sustainable Energy Rev.* **2014**, *35*, 109–125.
- [2] R. Schlögl, *Angew. Chem. Int. Ed.* **2019**, *58*, 343–348; *Angew. Chem.* **2019**, *131*, 349–354.
- [3] K. F. Kalz, R. Kraehnert, M. Dvoyashkin, R. Dittmeyer, R. Gläser, U. Krewer, K. Reuter, J.-D. Grunwaldt, *ChemCatChem* **2017**, *9*, 17–29.
- [4] S. Schiebahn, T. Grube, M. Robinus, V. Tietze, B. Kumar, D. Stolten, *Int. J. Hydrogen Energy* **2015**, *40*, 4285–4294.
- [5] R. Schlögl, *Angew. Chem. Int. Ed.* **2015**, *54*, 4436–4439; *Angew. Chem.* **2015**, *127*, 4512–4516.
- [6] F. Schüth, *Chem. Ing. Tech.* **2011**, *83*, 1984–1993.
- [7] M. Sterner, I. Stadler, *Handbook of Energy Storage*, Springer-Verlag, Berlin, Germany, **2019**.
- [8] C. Mebrahtu, F. Krebs, S. Abate, S. Perathoner, G. Centi, R. Palkovits, *CO₂ Methanation: Principles and Challenges in Horizons in Sustainable Industrial Chemistry and Catalysis*, Vol. 178 (Eds.: S. Albonetti, S. Perathoner, E. A. Quadrelli), Elsevier, **2019**, pp. 85–103.
- [9] P. Sabatier, J.-B. Senderens, *CR Acad. Sci. Paris* **1902**, *134*, 514–516.

- [10] F. Ocampo, B. Louis, L. Kiwi-Minsker, A. C. Roger, *Appl. Catal. A* **2011**, *392*, 36–44.
- [11] S. Rahmani, M. Rezaei, F. Meshkani, *J. Ind. Eng. Chem.* **2014**, *20*, 1346–1352.
- [12] G. Garbarino, P. Riani, L. Magistri, G. Busca, *Int. J. Hydrogen Energy* **2014**, *39*, 11557–11565.
- [13] H. Muroyama, Y. Tsuda, T. Asakoshi, H. Masitah, T. Okanishi, T. Matsui, K. Eguchi, *J. Catal.* **2016**, *343*, 178–184.
- [14] B. Mutz, A. M. Ganzler, M. Nachttegaal, O. Muller, R. Frahm, W. Kleist, J.-D. Grunwaldt, *Catalysts* **2017**, *7*, 279.
- [15] J. Ashok, M. L. Ang, S. Kawi, *Catal. Today* **2017**, *281*, 304–311.
- [16] C. Lv, L. Xu, M. Chen, Y. Cui, X. Wen, Y. Li, C.-e. Wu, B. Yang, Z. Miao, X. Hu, Q. Shou, *Front. Chem.* **2020**, *8*.
- [17] C. Mebrahtu, F. Krebs, S. Perathoner, S. Abate, G. Centi, R. Palkovits, *Catal. Sci. Technol.* **2018**, *8*, 1016–1027.
- [18] D. Pandey, K. Ray, R. Bhardwaj, S. Bojja, K. V. R. Chary, G. Deo, *Int. J. Hydrogen Energy* **2018**, *43*, 4987–5000.
- [19] L. R. Winter, E. Gomez, B. H. Yan, S. Y. Yao, J. G. G. Chen, *Appl. Catal. B* **2018**, *224*, 442–450.
- [20] M.-A. Serrera, K. F. Kalz, E. Saraci, H. Lichtenberg, J.-D. Grunwaldt, *ChemCatChem* **2019**, *11*, 5018–5021.
- [21] G. Giorgianni, C. Mebrahtu, M. E. Schuster, A. I. Large, G. Held, P. Ferrer, F. Venturini, D. Grinter, R. Palkovits, S. Perathoner, G. Centi, S. Abate, R. Arrigo, *Phys. Chem. Chem. Phys.* **2020**, *22*, 18788–18797.
- [22] A. I. Tsiotsias, N. D. Charisiou, I. V. Yentekakis, M. A. Goula, *Nanomaterials* **2020**, *11*, 28.
- [23] M. P. Andersson, T. Bligaard, A. Kustov, K. E. Larsen, J. Greeley, T. Johannessen, C. H. Christensen, J. K. Nørskov, *J. Catal.* **2006**, *239*, 501–506.
- [24] J. Sehested, K. E. Larsen, A. L. Kustov, A. M. Frey, T. Johannessen, T. Bligaard, M. P. Andersson, J. K. Nørskov, C. H. Christensen, *Top. Catal.* **2007**, *45*, 9–13.
- [25] D. Pandey, G. Deo, *J. Mol. Catal. A* **2014**, *382*, 23–30.
- [26] S.-H. Kang, J.-H. Ryu, J.-H. Kim, S.-J. Seo, Y.-D. Yoo, P. S. Sai Prasad, H.-J. Lim, C.-D. Byun, *Korean J. Chem. Eng.* **2011**, *28*, 2282–2286.
- [27] H. L. Huynh, J. Zhu, G. Zhang, Y. Shen, W. M. Tucho, Y. Ding, Z. Yu, *J. Catal.* **2020**, *392*, 266–277.
- [28] B. H. Yan, B. H. Zhao, S. Kattel, Q. Y. Wu, S. Y. Yao, D. Su, J. G. G. Chen, *J. Catal.* **2019**, *374*, 60–71.
- [29] T. Burger, S. Ewald, A. Niederdränk, F. E. Wagner, K. Köhler, O. Hinrichsen, *Appl. Catal. A* **2020**, *604*, 117778.
- [30] M.-A. Serrera, A. Gaur, J. Jelic, S. Weber, C. Fritsch, A. H. Clark, E. Saraci, F. Studt, J.-D. Grunwaldt, *Catal. Sci. Technol.* **2020**, *10*, 7542–7554.
- [31] M. Geske, O. Korup, R. Horn, *Catal. Sci. Technol.* **2013**, *3*, 169–175.
- [32] A. M. Gänzler, M. Casapu, A. Boubnov, O. Müller, S. Conrad, H. Lichtenberg, R. Frahm, J.-D. Grunwaldt, *J. Catal.* **2015**, *328*, 216–224.
- [33] J. S. Choi, W. P. Partridge, C. S. Daw, *Appl. Catal. B* **2007**, *77*, 145–156.
- [34] A. Urakawa, N. Maeda, A. Baiker, *Angew. Chem.* **2008**, *120*, 9396–9399; *Angew. Chem. Int. Ed.* **2008**, *47*, 9256–9259.
- [35] T. Hyakutake, W. van Beek, A. Urakawa, *J. Mater. Chem. A* **2016**, *4*, 6878–6885.
- [36] A. Urakawa, A. Baiker, *Top. Catal.* **2009**, *52*, 1312–1322.
- [37] O. Korup, S. Mavlyankariev, M. Geske, C. F. Goldsmith, R. Horn, *Chem. Eng. Process.* **2011**, *50*, 998–1009.
- [38] J. Kopycinski, T. J. Schildhauer, F. Vogel, S. M. A. Biollaz, A. Wokaun, *J. Catal.* **2010**, *271*, 262–279.
- [39] J. A. Hernandez Lalinde, K. Kofler, X. Huang, J. Kopycinski, *Catalysts* **2018**, *8*, 86.
- [40] J. A. Hernandez Lalinde, P. Roongruangsree, J. Ilsemann, M. Bäumer, J. Kopycinski, *Chem. Ing. J.* **2020**, *390*, 124629.
- [41] S. Rönisch, J. Schneider, S. Matthischke, M. Schlüter, M. Götz, J. Lefebvre, P. Prabhakaran, S. Bajohr, *Fuel* **2016**, *166*, 276–296.
- [42] D. Livio, C. Diehm, A. Donazzi, A. Beretta, O. Deutschmann, *Appl. Catal. A* **2013**, *467*, 530–541.
- [43] J. Sa, D. L. Fernandes, F. Aiouache, A. Goguet, C. Hardacre, D. Lundie, W. Naem, W. P. Partridge, C. Stere, *Analyst* **2010**, *135*, 2260–2272.
- [44] C. Diehm, O. Deutschmann, *Int. J. Hydrogen Energy* **2014**, *39*, 17998–18004.
- [45] R. Horn, O. Korup, M. Geske, U. Zavyalova, I. Oprea, R. Schlögl, *Rev. Sci. Instrum.* **2010**, *81*, 064102.
- [46] J. Toutou, K. Morgan, R. Burch, C. Hardacre, A. Goguet, *Catal. Sci. Technol.* **2012**, *2*, 1811–1813.
- [47] B. Mutz, P. Sprenger, W. Wang, D. Wang, W. Kleist, J.-D. Grunwaldt, *Appl. Catal. A* **2018**, *556*, 160–171.
- [48] J. Ren, H. L. Guo, J. Z. Yang, Z. F. Qin, J. Y. Lin, Z. Li, *Appl. Surf. Sci.* **2015**, *351*, 504–516.
- [49] B. Miao, S. S. K. Ma, X. Wang, H. B. Su, S. H. Chan, *Catal. Sci. Technol.* **2016**, *6*, 4048–4058.
- [50] C. Vogt, E. Groeneveld, G. Kamsma, M. Nachttegaal, L. Lu, C. J. Kiely, P. H. Berben, F. Meirer, B. M. Weckhuysen, *Nat. Catal.* **2018**, *1*, 127–134.
- [51] S. M. Kim, P. M. Abdala, T. Margossian, D. Hosseini, L. Foppa, A. Armutlulu, W. van Beek, A. Comas-Vives, C. Coperet, C. Muller, *J. Am. Chem. Soc.* **2017**, *139*, 1937–1949.
- [52] E. Monachino, M. Greiner, A. Knop-Gericke, R. Schlögl, C. Dri, E. Vesselli, G. Comelli, *J. Phys. Chem. Lett.* **2014**, *5*, 1929–1934.
- [53] A. Solis-Garcia, J. C. Fierro-Gonzalez, *J. Nanosci. Nanotechnol.* **2019**, *19*, 3110–3123.
- [54] Q. S. Pan, J. X. Peng, T. J. Sun, S. Wang, S. D. Wang, *Catal. Commun.* **2014**, *45*, 74–78.
- [55] P. A. U. Aldana, F. Ocampo, K. Kobl, B. Louis, F. Thibault-Starzyk, M. Daturi, P. Bazin, S. Thomas, A. C. Roger, *Catal. Today* **2013**, *215*, 201–207.
- [56] A. Westermann, B. Azambre, M. C. Bacariza, I. Graca, M. F. Ribeiro, J. M. Lopes, C. Henriques, *Catal. Today* **2017**, *283*, 74–81.
- [57] C. Schild, A. Wokaun, R. A. Koepfel, A. Baiker, *J. Phys. Chem.* **1991**, *95*, 6341–6346.
- [58] J. Ren, X. Qin, J.-Z. Yang, Z.-F. Qin, H.-L. Guo, J.-Y. Lin, Z. Li, *Fuel Process. Technol.* **2015**, *137*, 204–211.
- [59] M. Trenary, K. J. Uram, J. T. Yates, *Surf. Sci.* **1985**, *157*, 512–538.
- [60] J. C. Campuzano, R. G. Greenler, *Surf. Sci.* **1979**, *83*, 301–312.
- [61] K. A. Layman, M. E. Bussell, *J. Phys. Chem. B* **2004**, *108*, 10930–10941.
- [62] Z. Zhang, Y. Tian, L. Zhang, S. Hu, J. Xiang, Y. Wang, L. Xu, Q. Liu, S. Zhang, X. Hu, *Int. J. Hydrogen Energy* **2019**, *44*, 9291–9306.
- [63] S. I. Fujita, N. Takezawa, *Chem. Ing. J.* **1997**, *68*, 63–68.
- [64] J. Baltrusaitis, J. H. Jensen, V. H. Grassian, *J. Phys. Chem. B* **2006**, *110*, 12005–12016.
- [65] H. Li, J. Zhang, D. J. Young, *Corros. Sci.* **2012**, *54*, 127–138.
- [66] B. Mutz, M. Belimov, W. Wang, P. Sprenger, M.-A. Serrera, D. Wang, P. Pfeifer, W. Kleist, J.-D. Grunwaldt, *ACS Catal.* **2017**, *7*, 6802–6814.
- [67] *NIST Chemistry WebBook* (available at <https://webbook.nist.gov/>, accessed on 01.06.2020).
- [68] J.-D. Grunwaldt, N. van Vegten, A. Baiker, *Chem. Commun.* **2007**, 4635–4637.
- [69] O. Muller, M. Nachttegaal, J. Just, D. Lutzenkirchen-Hecht, R. Frahm, *J. Synchrotron Radiat.* **2016**, *23*, 260–266.
- [70] R. Frahm, *Rev. Sci. Instrum.* **1989**, *60*, 2515–2518.
- [71] D. E. Doronkin, H. Lichtenberg, J.-D. Grunwaldt, *Cell Designs for In Situ and Operando Studies in XAFS Techniques for Catalysts, Nanomaterials, and Surfaces* (Eds.: Y. Iwasawa, K. Asakura, M. Tada), Springer International Publishing, Cham, **2017**, pp. 75–89.
- [72] O. Deutschmann, *Modeling and Simulation of Heterogeneous Catalytic Reactions*, Wiley-VCH Verlag GmbH & Co. KGaA, **2011**.
- [73] A. H. Clark, J. Imbao, R. Frahm, M. Nachttegaal, *J. Synchrotron Radiat.* **2020**, *27*, 551–557.
- [74] B. Ravel, M. Newville, *J. Synchrotron Radiat.* **2005**, *12*, 537–541.

Manuscript received: April 3, 2021
Revised manuscript received: May 2, 2021
Accepted manuscript online: May 6, 2021
Version of record online: June 1, 2021